Supplementary Information for

Nature and Distribution of Stable Subsurface Oxygen in Copper Electrodes During Electrochemical CO₂ Reduction

Filippo Cavalca, [1,2] *Rafael Ferragut,* [3,4] *Stefano Aghion,* [3,4] *André Eilert,* [1,2,5] *Oscar Diaz-Morales,* [1] *Chang Liu,* [1] *Ai Leen Koh,* [6] *Thomas W. Hansen,* [7] *Lars G. M. Pettersson,* [1] *and Anders Nilsson* [*,1]

[1]   Department of Physics, AlbaNova University Center, Stockholm University, S-10691 Stockholm, Sweden

[2]   SLAC National Accelerator Laboratory, 2575 Sand Hill Road, Menlo Park, California 94025, USA

[3]   LNESS Laboratory and Dipartimento di Fisica, Politecnico di Milano, Via Anzani 42, 22100 Como, Italy

[4]   Istituto Nazionale di Fisica Nucleare, via Celoria 16, 20133 Milano, Italy

[5]   SUNCAT Center for Interface Science and Catalysis, Department of Chemical Engineering, Stanford University, 443 Via Ortega, Stanford, CA 95305, USA

[6]   Stanford Nano Shared Facilities, Stanford University, 348 Via Pueblo, Stanford, CA 94305, USA

[7]   Center for Electron Nanoscopy, Technical University of Denmark, Fysikvej 307, 2800 Kgs. Lyngby, Denmark

Corresponding Author

[*]Stockholm University, Chemical Physics, 10691 Stockholm, Sweden. Email: andersn@fysik.su.se

S1. Electrochemistry

The electrochemical treatment for both TEM and PAS samples is described in Figure S1. During the first cycle (black line in in Figure S1a), the potential was swept negatively from open circuit potential (OCP) to -1.15 V vs RHE, then back to 0.1 V vs RHE. During the following 4 cycles the potential was swept between -1.15 and 0.1 V vs RHE. Subsequently, the potential was swept between -1.15 and 0.7 V vs RHE in order to oxidize the sample. As shown by the CV in Figure S1b, Cu oxidation occurs from an onset potential of +0.6 V, and the Cu reduction wave is observed between -0.3 and -0.5 V in the cathodic sweep. During the tenth reduction cycle, the potential sweep was interrupted at -1.15 V vs RHE and held for 55 minutes, as shown in Figure S1c.
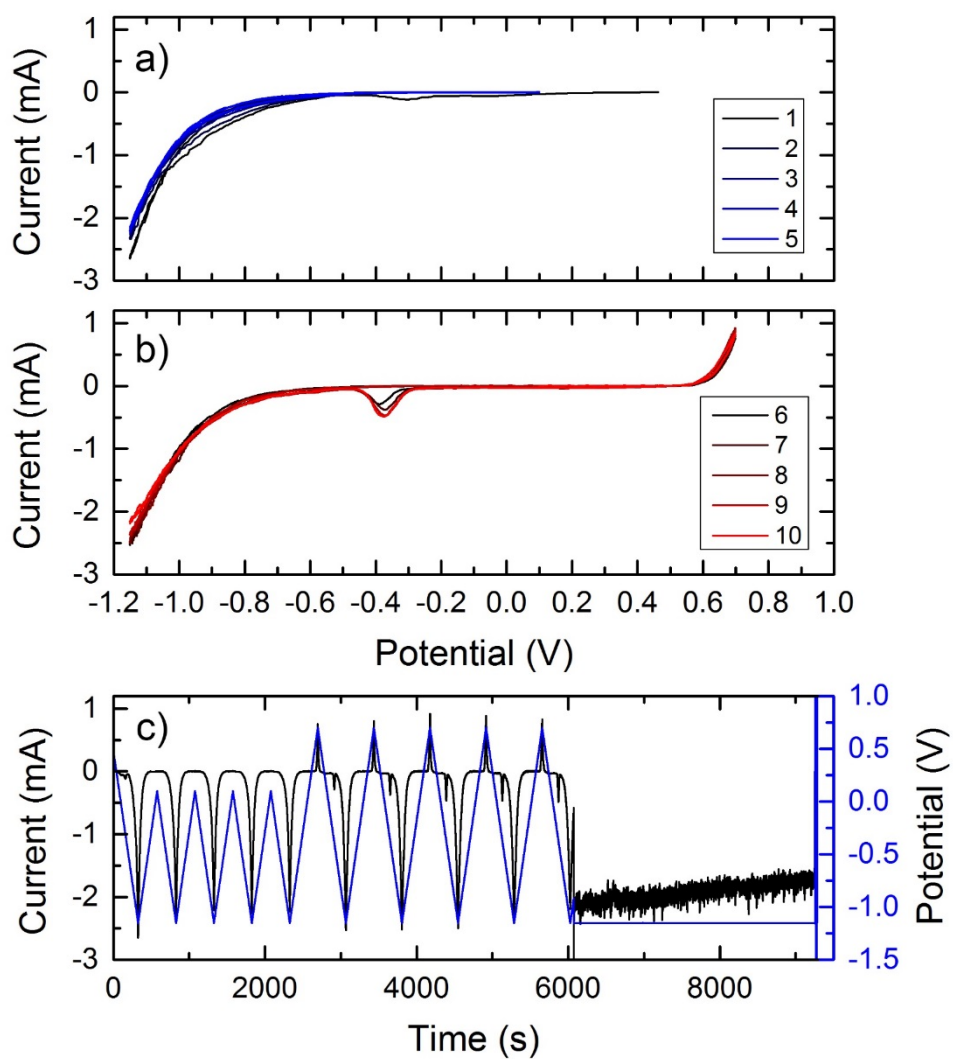
Figure S1. All potentials are reported vs RHE. (a) Electrochemical cyclic voltammogram (CV) of (b) the first 5 reduction cycles on the sample and (c) the following 5 oxidation-reduction cycles.

S2.   Scanning electron microscopy

The electrochemical oxidation and reduction modifies the sample appearance, as can be seen in Figure S2. Scanning transmission electron microscopy (SEM) of a freshly prepared TEM grid with Cu NPs is shown in Figure S2a. The grid openings are sharp and well defined, and nanoparticles adhering to the opening edges can be seen. In Figure S2b the OD-Cu sample after TEM investigation is shown. After electrochemical treatment, the grid edges appear smooth and rounded, whereas nanoparticles clustered on the grid surface as well as on the opening edges are visible. A high magnification image of Cu NPs attached to the edge of the grid is shown in Figure S2c. The smoothening of the grid edges and the presence of nanoparticles attached over the entire sample surface in Figure S2b indicate that copper undergoes electrochemical etching and material redeposition. Etching is known to happen during oxidation, where Cu is dissolved and redeposited, subsequently transforming into Cu_2O.[1,2] It is possible that sharp features, such as edges on the metallic grid act as electric field enhancers, thereby locally intensifying the etching phenomenon and causing the smoothening of such features.
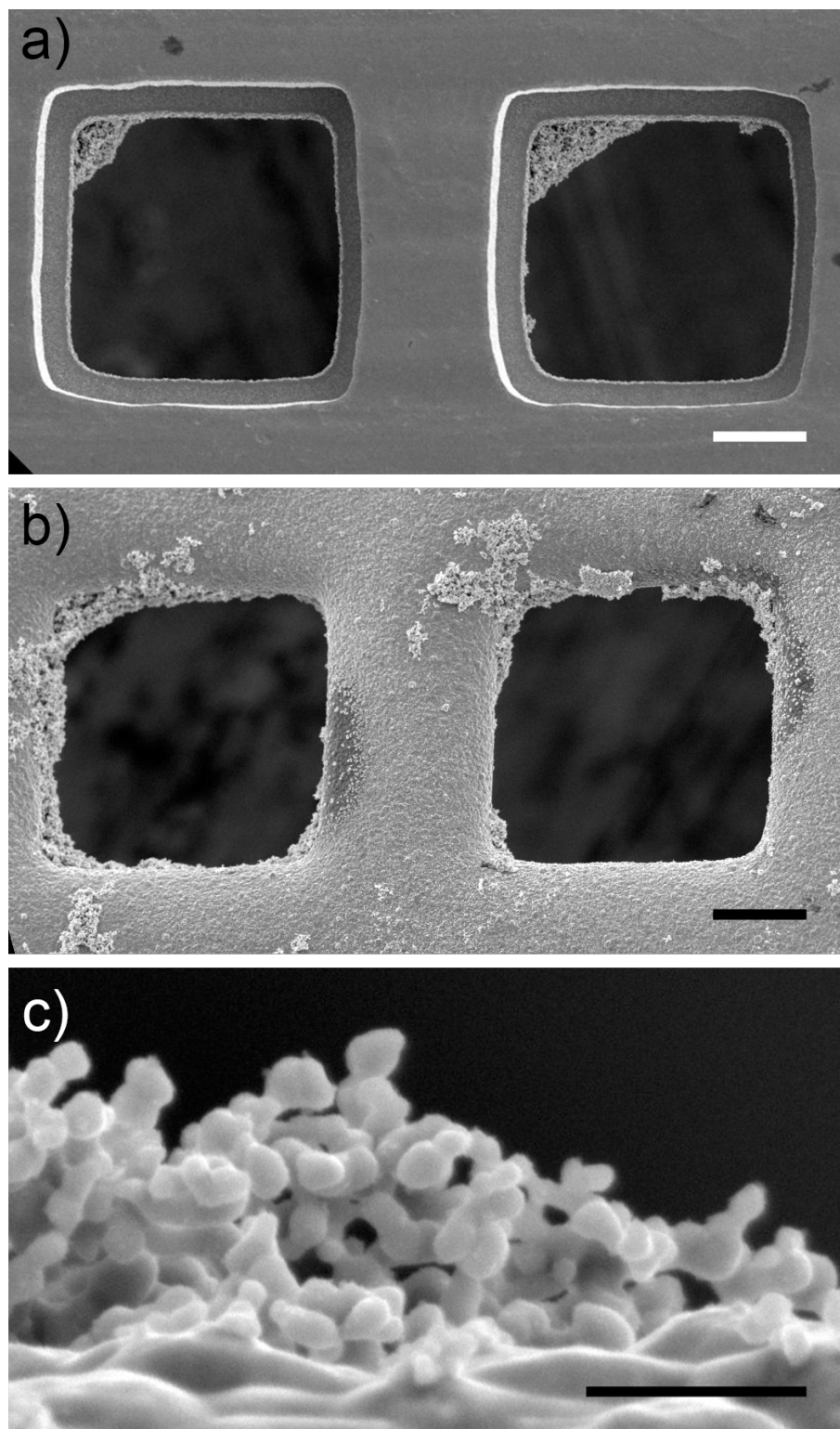
Figure S2. Scanning electron microscopy (SEM) images of (a) the as prepared TEM sample, (b-c) the OD-Cu sample after TEM investigation. The scale bar in (a) and (b) is 10 μm, and in (c) is 500 nm. Images were acquired with an acceleration voltage of 5 kV in secondary

electron imaging mode. The sample was exposed to air during the transfer to the SEM (~1 minute).

Copper foils for PAS were treated following the same electrochemical procedure as for the TEM sample. After analysis, the samples were cross-sectioned using a Jeol SM09010 Cross Section Polisher operated for 12 hours with an Ar-ion beam generated using a voltage of 5kV, and a beam current of 90-100 mA. Samples were analyzed using a JEOL JSM-7000F SEM. A top view of the oxidized sample is shown in Figure S3a, where CuCubes of 20-80 nm lateral size are visible.[3] Cross-sectional SEM images of the oxidized and the OD-Cu samples are shown in Figure S3b and Figure S3c, respectively. From the cross sections, the thickness of the nanostructured layer and the pore size can be estimated. The thickness of both oxidized and OD-Cu samples is 0.1-3 µm. For the oxidized sample, the cube size is 30-90 nm and the pore size is 10-100 nm. For the OD-Cu sample, the cube size is 20-60 nm and the pore size is 5-50 nm. The OD-Cu sample is therefore less porous and the nanostructures have less well-defined morphology than the oxidized sample. Besides, the OD-Cu sample exhibits large voids between the nanostructured layer and the pristine Cu substrate, up to 1 µm in size. Interestingly, the nanostructures facing the voids are considerably larger than those in the bulk of the nanostructured layer. This suggests that either shrinking of the oxidized layer occurs during reduction or the electrochemical conditions, such as the local pH and electrolyte composition, are different in the $Cu-Cu_2O$ interface, causing etching. The presence of such voids might also have an effect during CO_2RR.

These measurements were used to compute the diffusion length of positrons in the different samples.
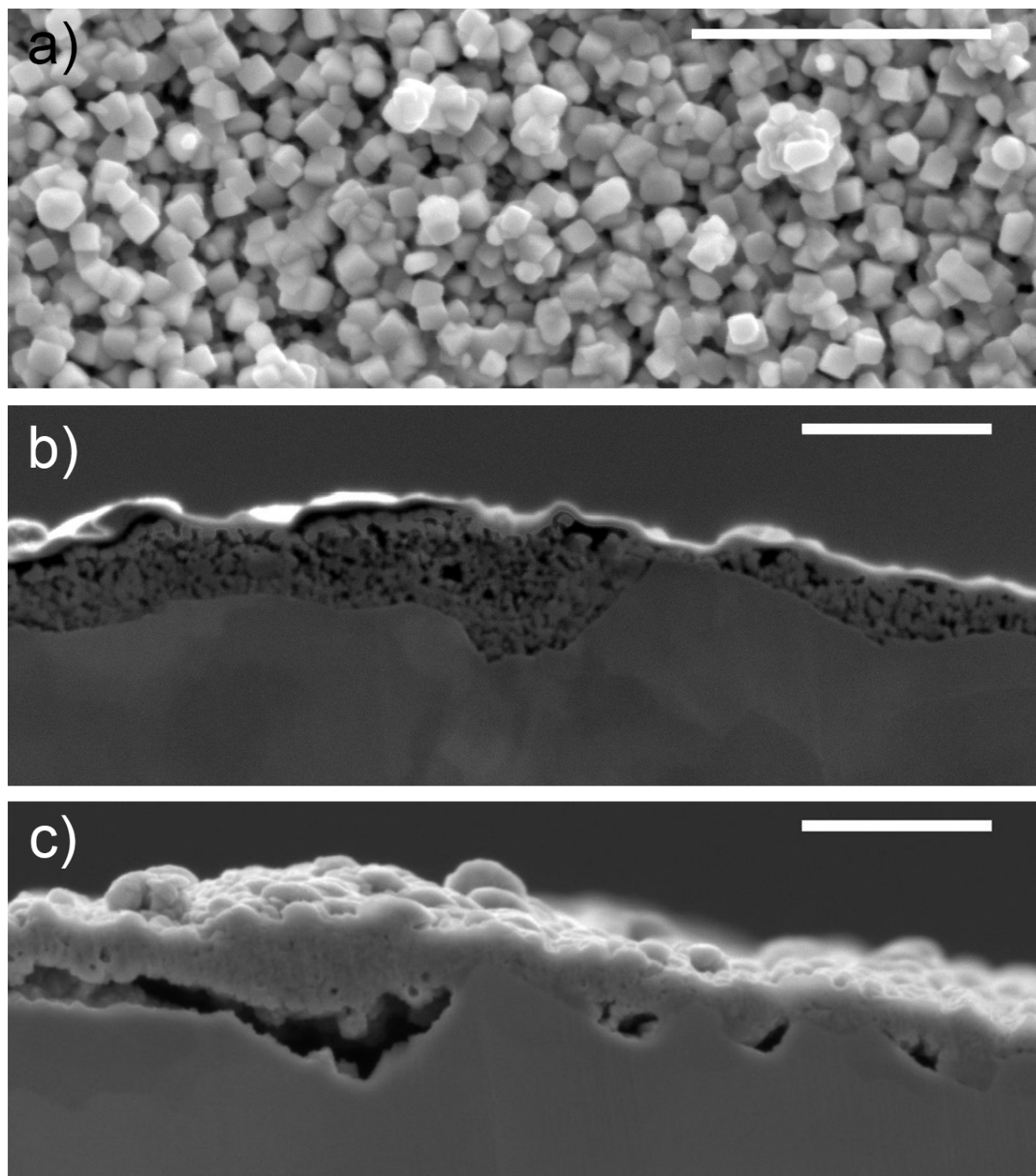
Figure S3. SEM images of EC-treated Cu foils for PAS analysis. Acceleration voltage 5 kV, scale bars are 1 μm. (a) Top view of oxidized sample. (b) Cross-sectional view of oxidized sample. (c) Cross-sectional view of OD-Cu reduced sample.

S3. Transmission electron microscopy

Additional images of the OD-Cu sample are shown in Figure S4. The amorphous layer is visible in all frames.
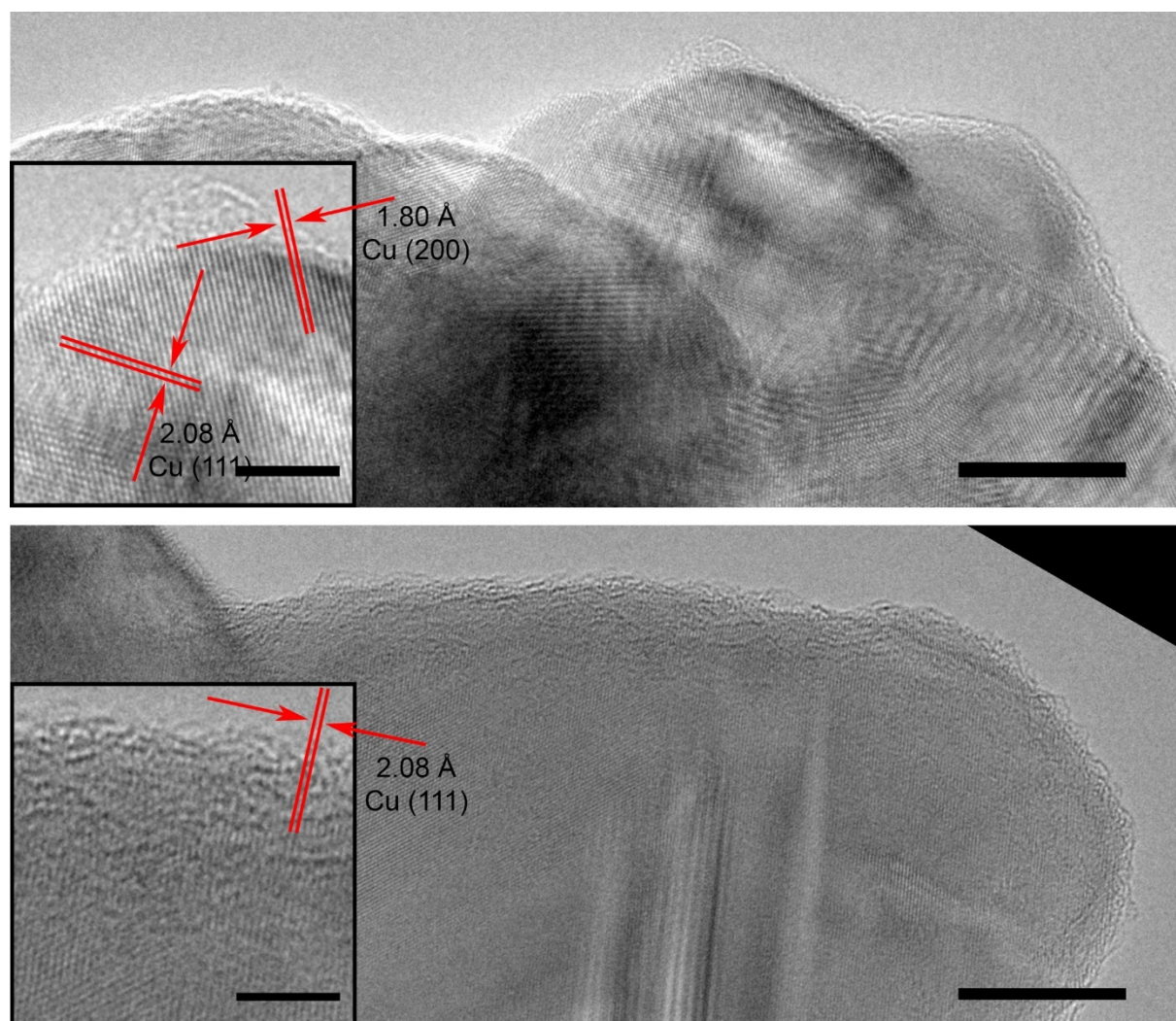

Figure S4. Quasi in situ high resolution transmission electron microscopy (HRTEM) images of the OD-Cu sample. The sample was never in contact with air from the electrochemical treatment to the acquisition of these images. Scale bars of main frames are 10 nm, scale bars of insets are 3 nm.

In Figure S5, TEM images of the as-received Cu NPs are shown. Lattice fringes from the Cu_2O (111) and (200) planes are resolved, corresponding to a d-spacing of 2.46 and 2.13 Å,

respectively. Lattice fringes are visible throughout the particles and up to the surface, indicating that the particle surface is crystalline and not amorphous.
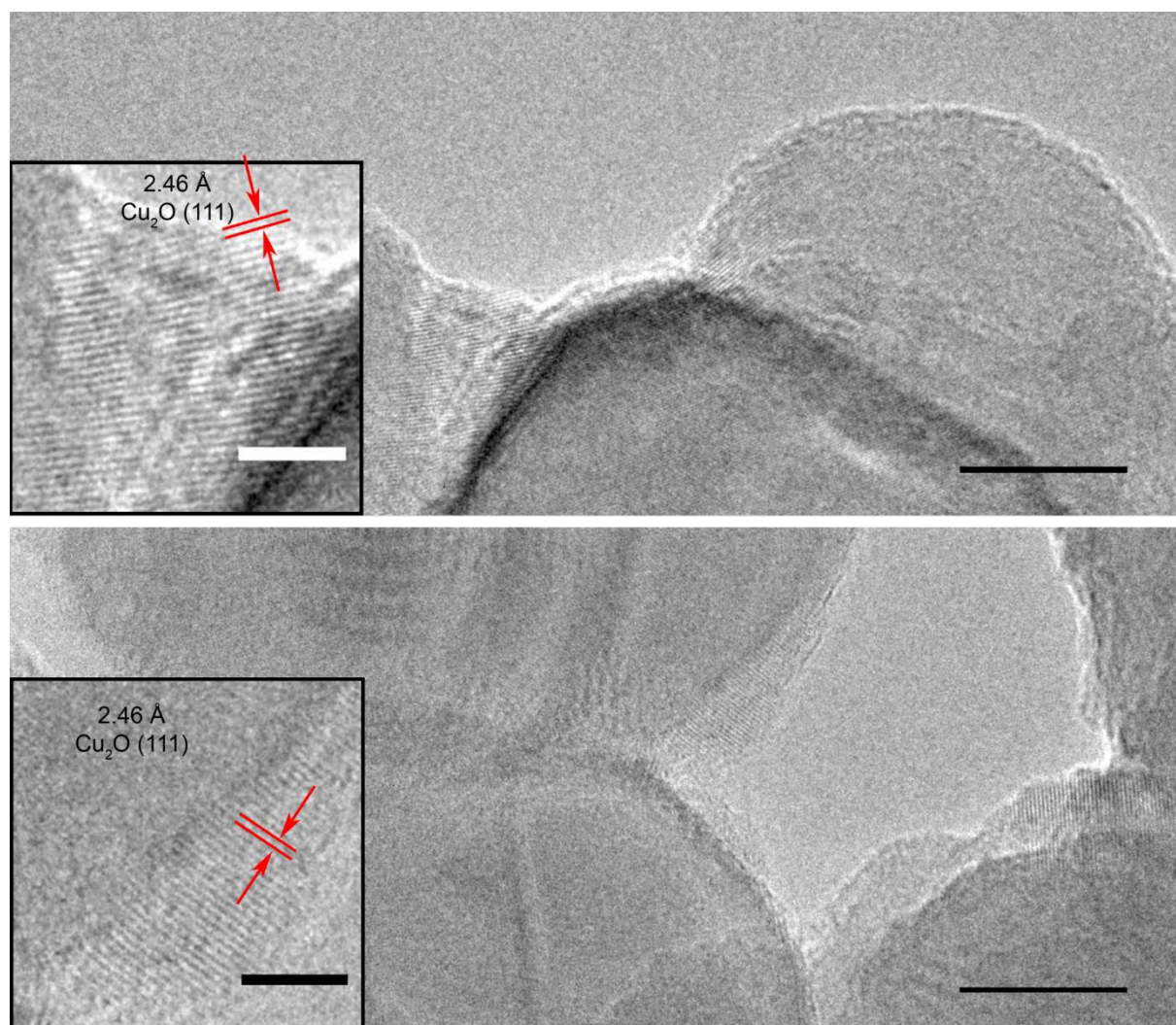
Figure S5. TEM images of the as-received copper nanoparticles. Scale bars of main frames are 10 nm, scale bars of insets are 3 nm. Lattice fringes from the Cu₂O (111) planes are resolved up to the surface of the particles.

STEM EELS was performed on 30 OD-Cu particles after 1 h under CO_2RR conditions at -1.15 V vs RHE. Relative elemental quantification was performed on spectra using integral methods, allowing to obtain atomic ratios between Cu and O.[4] All spectra were analyzed with the same parameters to standardize the results. Specifically, the energy window for background fitting preceding the O *K*-edge was chosen to start at 460 eV with a width of

ΔE=50 eV, while that for Cu was chosen to start at 870 eV with a width of ΔE=50 eV. Beam-induced carbon deposition was observed during STEM EELS acquisition, as is common when the sample and/or the sample holder are not properly cleaned using, *e.g.*, O_2/Ar plasma prior to analysis. Any cleaning procedure other than rinsing with water (Experimental methods section in the main text) was deliberately avoided in order not to contaminate, oxidize or alter the sample. However, carbon contamination was negligible and, importantly, no correlation between the C *K*- and O *K*-edge EELS signals could be identified (Figure S6). This indicates that the carbon contamination was deposited by the beam and was oxygen-free. Additional data is shown in Figure S7 and Figure S8.
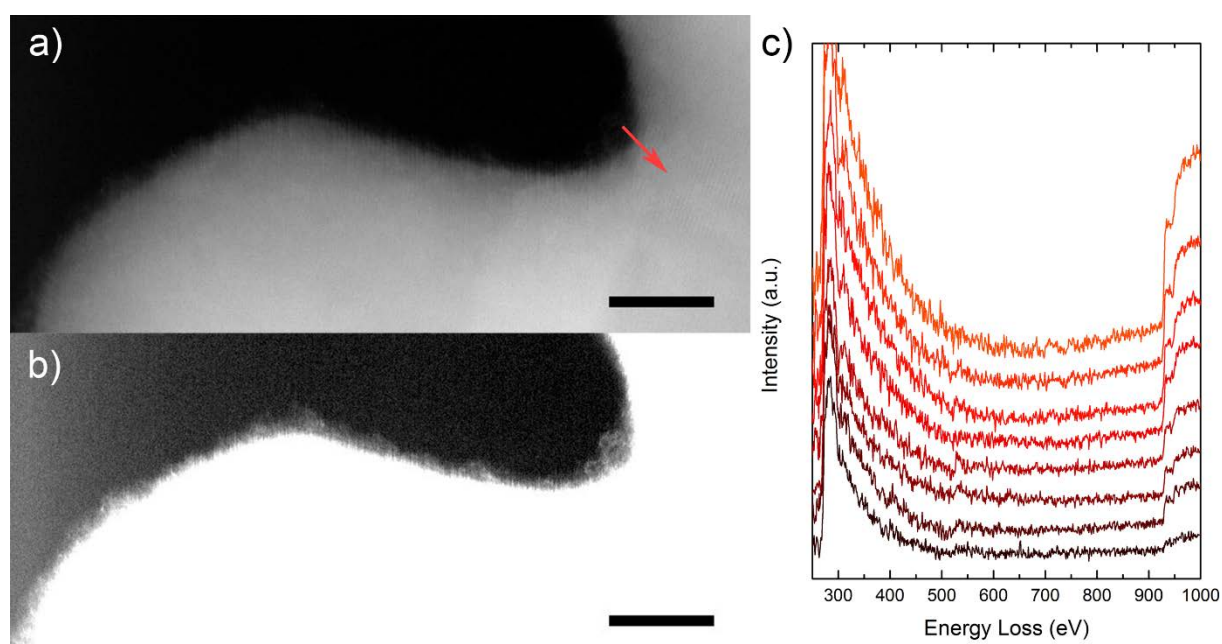

Figure S6. (a) STEM ADF image of an OD-Cu NP after 1 h potentiostatic hold at -1.15 V vs RHE. (b) Contrast-enhanced version of (a), highlighting the amorphous layer. Scale bars are 10 nm. (c) STEM EEL spectra acquired at evenly spaced points along the arrow indicated in (a,b).

Figure S7. (a) STEM ADF image of an OD-Cu NP after 1 h potentiostatic hold at -1.15 V vs RHE. (b) Contrast-enhanced version of (a), highlighting the amorphous layer. Scale bars are 10 nm. (c) STEM EEL spectra acquire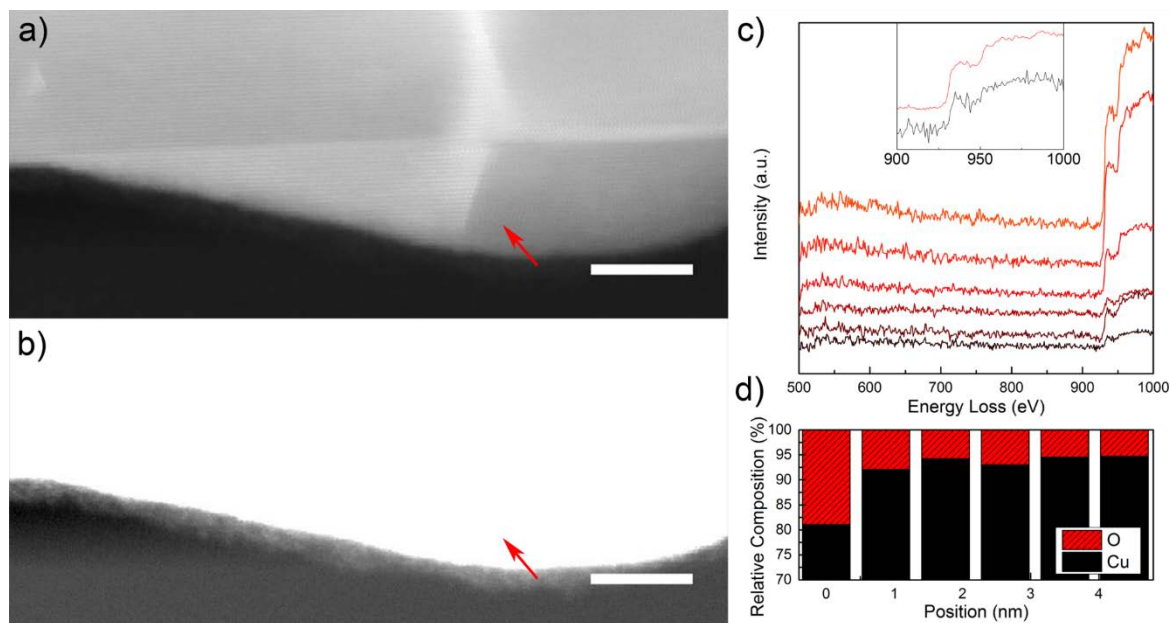d at evenly spaced points along the arrow indicated in (a,b) and inset showing the Cu-L edge of the first and last spectra, acquired in the amorphous layer and in the bulk of the NP, respectively. (d) Elemental quantification obtained from the spectra in (c).

Figure S8 (a) STEM ADF image of an OD-Cu NP after 1 h potentiostatic hold at -1.15 V vs RHE. (b) Contrast-enhanced version of (a), highlighting the amorphous layer. Scale bars are 10 nm. (c) STEM EEL spectra acquired along the arrow indicated in (a,b) and inset showing the Cu-L edge of the first and last spectra, acquired in the amorphous layer and in the bulk of the NP, respectively. (d) Elemental quantification obtained from the spectra in (c).
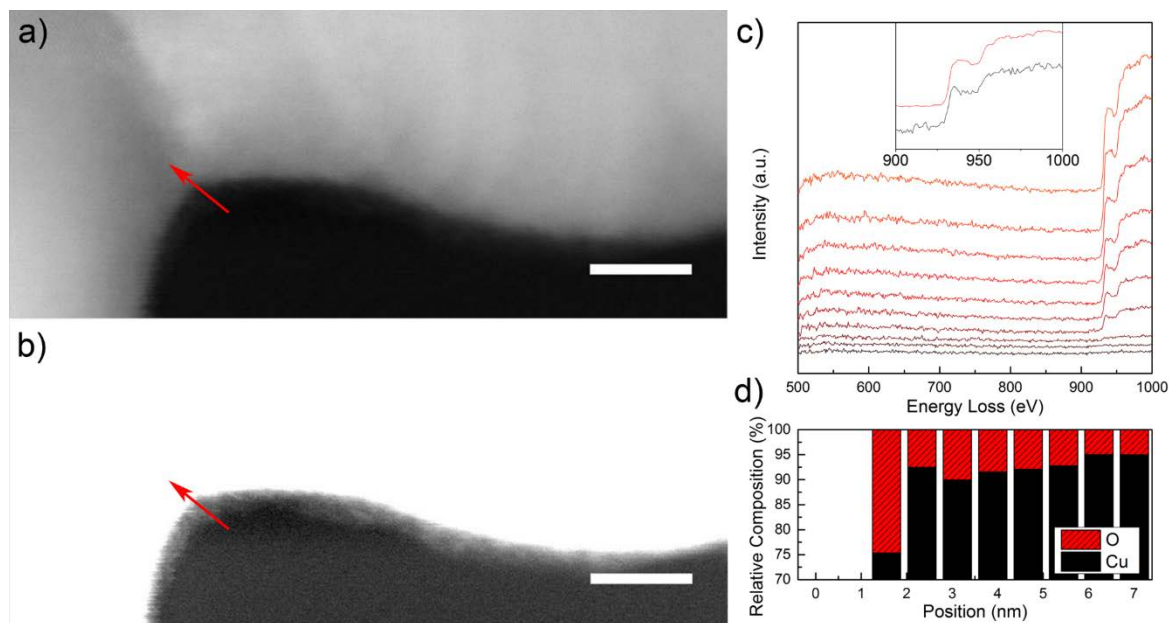
S4.   Positron annihilation spectroscopy

S4.1.   Depth profiling

The depth-resolution of a variable-energy positron beam depends on the positron implantation profiles obtained by the so-called Makhov distribution and the exploring region of positron and positronium.[5] Figure S9 shows the implantation profiles for Cu (continuous lines) and Cu_2O (dashed lines) at four implantation energies (1, 3, 5 and 10 keV). The Makhov distribution is sharp at low positron implantation energy and broader at high implantation energy (Figure S9). The exploring region after implantation depends on the positron and positronium diffusion length. In particular, the average positron diffusion length in Cu with a low defect concentration is of the order of 100 nm, whereas in Cu_2O it is limited to about 20 nm.
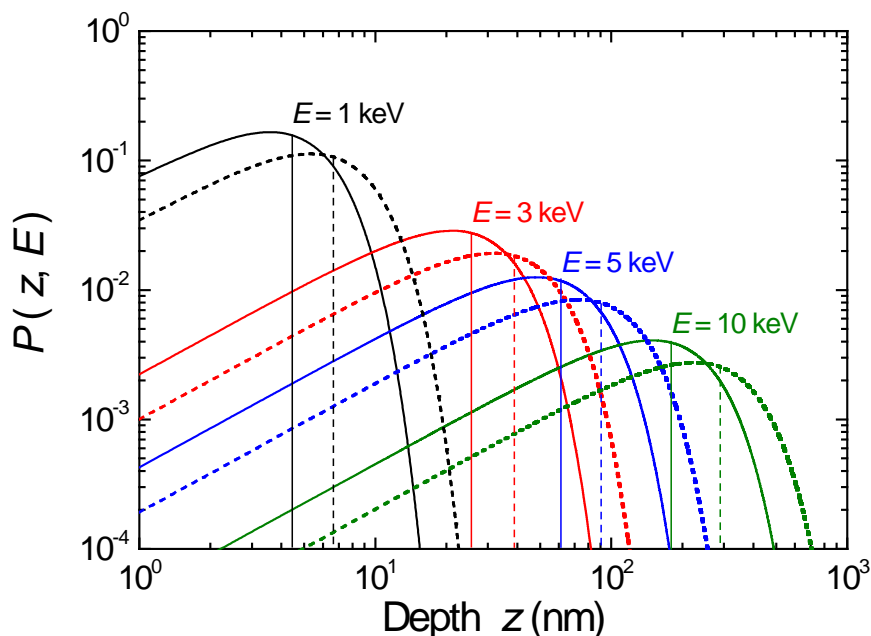

Figure S9 Makhov implantation profiles for Cu (continuous lines) and Cu_2O (dashed lines) for different implantation energies: 1, 3, 5, and 10 keV (distributions in black, red, blue and

green, respectively). The vertical continuous (Cu) and dashed (Cu₂O) lines indicate the

average depth reached by positrons for each energy.

S4.2.   S-parameter

The S-parameter corresponds to the area of the annihilation peak within the $|E - 511 \text{ keV}| \leq 0.85 \text{ keV}$ ($p_L \leq 0.456$ atomic units) energy region. In order to interpret the S-parameter plot (Fig. 3a), it is important to understand where the positrons annihilate. To do so, for the present case, one has to consider both the sample morphology (Fig. S3) and the fraction of positrons annihilating in each layer of the sample (Fig. 3b). Regarding the morphology, in the oxidized sample a layer with average thickness of 600 nm of Cu_2O nanoparticles with a lateral dimension of 60 ± 30 nm was observed (Fig. S3b). After reduction (OD-Cu sample), the Cu_2O layer was replaced with a Cu-rich layer of nanoparticles having a smaller lateral size of 40 ± 20 nm and average thickness of 400 nm (Fig. S3c). For the estimation of the fraction of positrons in the NPs film, a model based on the VEPFIT software was used (see VEPFIT section S4.3).[6] The VEPFIT software is a best-fit procedure based on the solution of the diffusion equation for positrons in each layer of a heterostructure, taking into account the energy-dependent positron implantation profiles (Fig. S9).[5] To fit the experimental data, a three-layers model was used comprising of an external surface (*i.e.* the sample/vacuum interface) a layer formed by nanoparticles, and a copper substrate. The continuous lines through data points in Fig.3a represent the best fits. Dashed lines in Fig. 3b show that for all samples, the positrons implanted at low energy tend to migrate to the external sample/vacuum interface where they mainly form positronium (see Fig. S10). The continuous lines in Fig. 3b show that more than 75% of the positrons annihilate within the film of nanoparticles at energies between 1.5 and 9 keV in the oxidized sample and between 1 and 7 keV in the OD-Cu sample, respectively. At high implantation energies, positrons tend to annihilate into the Cu substrate in all samples (dash-dotted lines in Fig. 3b).

In order to obtain insight about the preferred annihilation sites within the NP layers, *i.e.* if the positrons tend to annihilate either within the bulk of the NPs or in their surface and subsurface, an estimation of the positron diffusion length in each material was performed. The positron diffusion length in the as-received defect-rich Cu sample, estimated with VEPFIT, is about 100 ± 10 nm. On the contrary, in the oxidized film, the positron diffusion length is 15 ± 5 nm, that is approximately half of the lateral size of the Cu_2O NPs (Fig. S3). It was possible to estimate using Eq. 3 (Sec. S4.6) that in the oxidized sample about ¾ of the implanted positrons annihilate inside the Cu_2O cubes, and the remaining positrons annihilate at the surface of the NPs, which has the same composition. Therefore, for the oxidized sample almost all positrons implanted between 2.8 and 7 keV annihilate in a Cu_2O environment (region between red arrows in Fig. 3a that corresponds to the maximum of the continuous red line in panel b). The situation for the reduced sample is different. Based on TEM observations (Figs. 2 and S4), the inner part of the OD-Cu NPs is crystalline Cu, where positrons can diffuse as far as several tens of nanometers as mentioned before for the as-received sample. However, in this case, the positron diffusion length is limited by the dimension of the nanoparticles (20 ± 5 nm), and positrons easily reach the NPs defect-rich subsurface. In this scenario, almost all positrons implanted into the reduced OD-Cu NPs ($\leq 94\%$), with kinetic energy between 1.8 and 4 keV (region between blue arrows in Fig. 3a), migrate and annihilate at the NPs subsurface providing information on its chemical environment. Positronium formation is not observed into the porous volume between the nanoparticles (see Fig. S10, between ~2 and 4 keV), but a possible contribution of para-Ps annihilation in the S-parameter in this range of energies cannot be excluded.

S4.3.   VEPFIT

VEPFIT enables a best-fit procedure based on the solution of the diffusion equation for positrons in each layer of a heterostructure, taking into account the energy-dependent positron implantation profiles (Makhov profiles).[5] For each layer in the modelled sample, a set of parameters is defined: the S-parameter, the positron diffusion length, the layer thickness and the layer density. To fit the experimental data, a three-layer model was used comprising the sample/vacuum interface, a layer formed by nanoparticles, and the copper substrate. The continuous lines through data points in Fig. 3a and b represent the best fits. On the basis of the thicknesses determined using SEM (Figs. S3b and c), a density of about 4 ± 1 and 5 ± 1 g/cm^3 was estimated using VEPFIT for the oxidized and OD-Cu films, respectively. The porosity of the films (rate between porous and total volume V_P/V_T) was estimated to be around 30-50%.

S4.4.   Positronium fraction

The positronium fraction[7] was measured and correlated with the fraction of positrons that diffuse and annihilate at the catalyst/vacuum interface (Fig. 3c).

The positron-electron bound state is called positronium. Positronium (Ps) is the lightest atom, about 2×10^{-3} times lighter than hydrogen, and exists in the ground state in two energetic sublevels: 25% singlet (para-Ps) and 75% triplet (ortho-Ps), according to the spin-coupling of the electron and positron. The annihilation features of the two positronium varieties in vacuum are different: para-Ps annihilates with emission of two gamma rays (511 keV each, similar to free annihilation without Ps formation), while ortho-Ps annihilates with emission of three gamma rays producing a continuous energy distribution between 0 and 511 keV with combined total energy equal to 1022 keV. Ps fraction measurements were performed using the "3γ-method".[7] In this method, the following ratio is defined:

$$R(E) = V/P \qquad\qquad (1)$$

where V is the integral of the annihilation spectrum in the energy range 350 keV up to 500 keV, mainly due to ortho-Ps annihilation, and P is the integral in the range 511±4.25 keV, mainly due to free and para-Ps annihilation.

"Pick-off" annihilation occurs when the positron of the ortho-Ps annihilates with an electron of the material (instead of the ortho-Ps electron) in relative singlet state emitting two γ-rays (instead of three).[8] When pick-off annihilation is negligible, the Ps fraction $F_{3\gamma}$ (E) can be obtained from $R(E)$ using the relationship:

$$F_{3\gamma} = \left[1 + \frac{P_1}{P_0}\left(\frac{R_1 - R(E)}{R(E) - R_0}\right)\right]^{-1}$$

(2)

where P_0 and R_0 are the values of the P- and R-parameters when the Ps fraction is zero ($F_{3\gamma}=0$), and P_1 and R_1 are the values of the P- and R-parameters when 100% of the positrons are bound as positronium ($F_{3\gamma}= 1$). Such calibration values for 0% and 100% Ps were measured in vacuum using a Ge (100) single-crystal at 1000 K.[7]

A plot of the Ps fraction (Figure S10) shows that 20-30% of Ps is formed near or at the sample/vacuum interface of every sample (*i.e.* in the subsurface region of the catalyst or at the Cu surface in the case of the as-received sample). The $F_{3\gamma}$ distribution follows the same trend as the distribution of positrons and Ps atoms that annihilate near or at the sample/vacuum interface (dashed line in Fig. 3c). The as-received sample produces more Ps at energies below 0.3 keV (at the vacuum interface),[9] whereas between ~0.4 and ~1.5 keV the Ps production seems to be higher in the oxidized and OD-Cu samples.
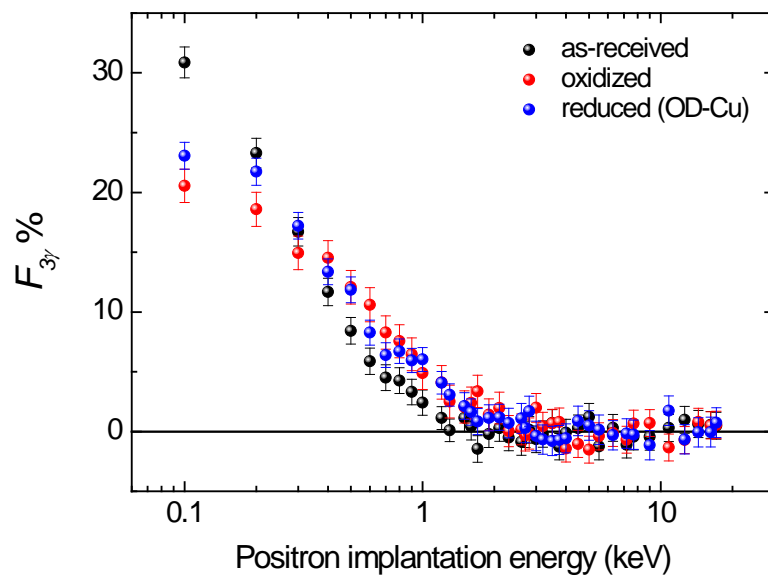
Figure S10. Depth profile of the Ps fraction $F_{3\gamma}$ in the oxidized (red), OD-Cu (blue), and as-received (black) samples.

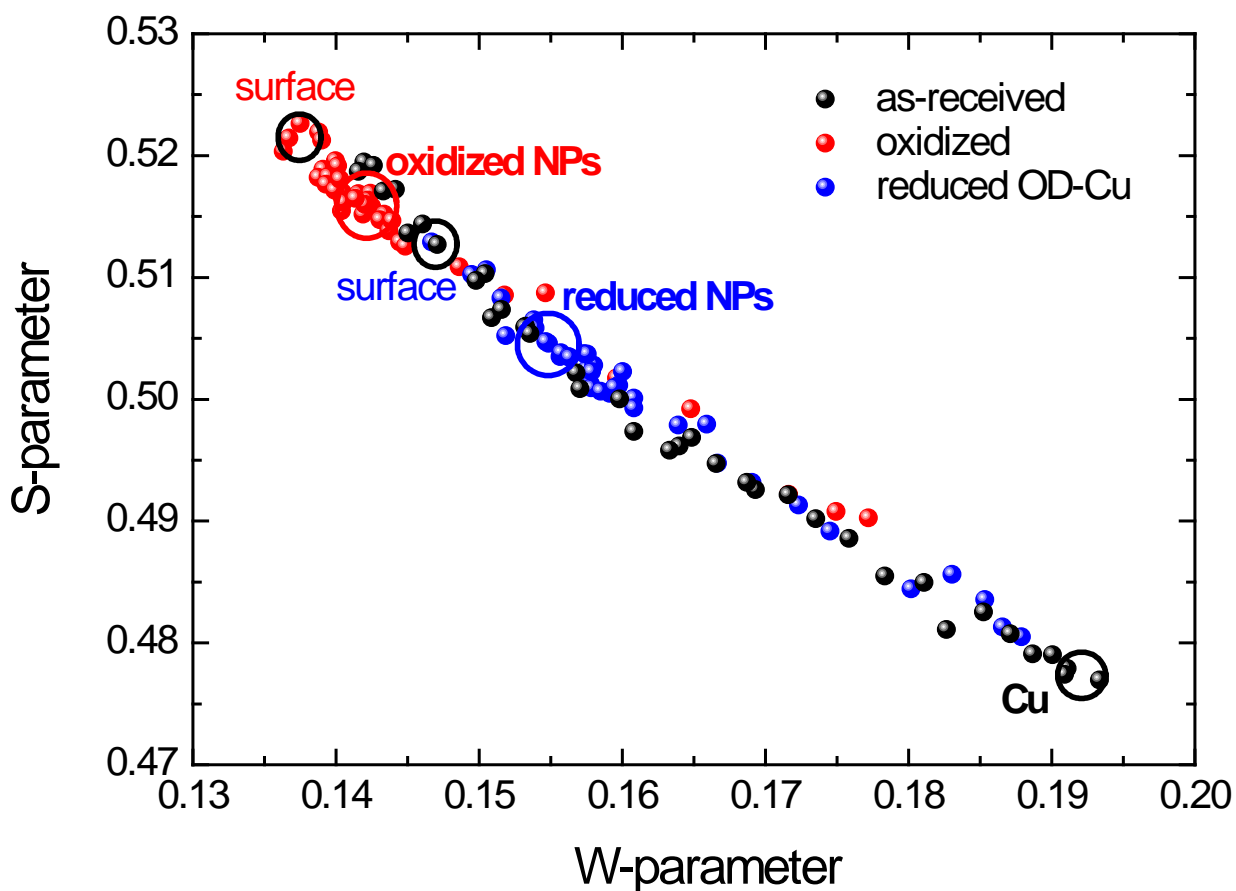## S4.5.   Relationship between S- and W-parameters

Figure S11. S-parameter vs. W-parameter plot (data of Fig. 3).

The relationship between the S-parameter obtained for the data in Fig. 3 and the W-parameter is shown in Figure S11. The evolution of both parameters from the surface down into the Cu substrate (black circles) can be followed. Two additional "poles" are found in the reduced OD-Cu and in the oxidized samples with respect to the values of W and S associated with the NPs. It is important to note that at the sample/vacuum interface the S-parameter (W-parameter) has a higher (lower) value than the value associated with the NPs. The increment (reduction) is due to formation of Ps, that tends to be maximum at the sample/vacuum interface, as shown in Figure S10.

S4.6. Langevin function

The parameter η describes the probability of an annihilation event inside a nanoparticle, and it depends on the ratio of the diameter d of the particle and the positron diffusion length L_+ inside the NP, according to the Langevin function:[10]

$$\eta = \coth\left(d/L_+\right) - L_+/d \qquad (3)$$

S4.7. Linear combination of the momentum distributions

With the aim to study the chemical environment near defects in OD-Cu, a linear combination between the momentum distributions of Cu (ρ_{Cu}) and Cu_2O (ρ_{Cu_2O}) was performed. However, the best fit does not reproduce well the distribution of OD-Cu (see Figure S12, χ^2/degree of freedom≈ 6).[11] The residual momentum distribution has similar characteristics to that of cupric oxide CuO reported by Druzhkov *et al.*[12] The intensity of such residual distribution, expressed as the ratio to the Cu distribution, i.e. ρ_{CuO}/ρ_{Cu} (Fig. 4c), is reduced by a factor 6 with respect to Ref.[12]. This was calculated taking into account the different instrumental resolutions used in the cited reference and in the present work. A new attempt of linear combination is shown in Figure S12a, including ρ_{CuO}, and it reproduces well the momentum distribution of OD-Cu (χ^2/degree of freedom≈ 1):

$$\rho_{OD-Cu} = \alpha\rho_{Cu} + \beta\rho_{Cu_2O} + \gamma\rho_{CuO} \qquad (4)$$

where α, β, and γ are the weights of the first neighbors of Cu, Cu_2O, and CuO, respectively.[13] Rearranging Eq. (4), we obtain the following overdetermined equation system:

$$\begin{bmatrix} \alpha \\ \beta \\ \gamma \end{bmatrix} = \begin{bmatrix} \cdots \\ \rho_{jOD-Cu} \\ \cdots \end{bmatrix} \Big/ \begin{bmatrix} \cdots & \cdots & \cdots \\ \rho_{jCu} & \rho_{jCu_2O} & \rho_{jCuO} \\ \cdots & \cdots & \cdots \end{bmatrix} \qquad (5)$$

To obtain α, β, and γ, the system in Eq. (5) was solved using an algorithm in the software MATLAB® capable of inverting the matrix containing the reference momentum distributions to obtain the unknowns.[13] Constraining the sum $\alpha + \beta + \gamma = 1$, the solution yields the values $\alpha = 0.18$, $\beta = 0.70$, and $\gamma = 0.12$ with an error around ± 0.05. This indicates that near 12% of the defects in OD-Cu have an oxygen concentration as high as Cu:O=1:1, whereas ~70% is in a concentration of approximately Cu:O=2:1.
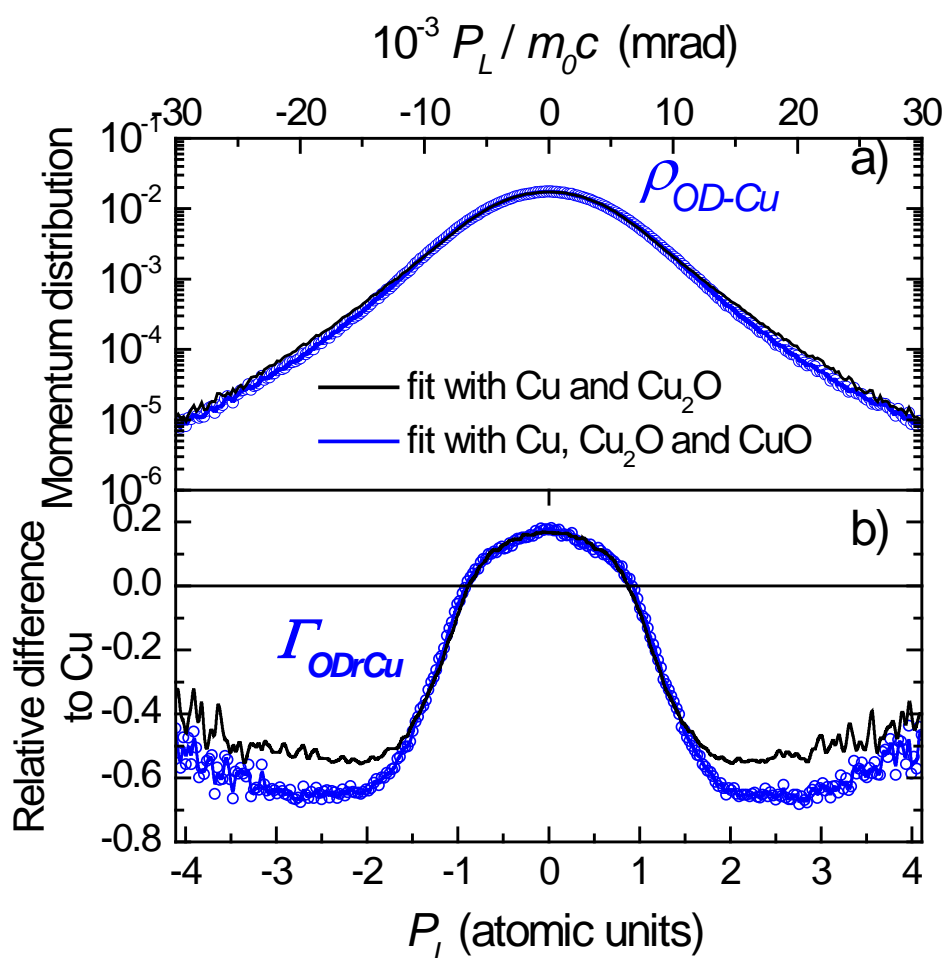

Figure S12. (a) CDB momentum distribution of the reduced OD-Cu sample (blue symbols). (b) Relative difference of the momentum distribution of reduced OD-Cu with respect to Cu. The continuous black and blue lines represent the linear fits with two and three terms, respectively (see text).

Figure S12b shows the relative difference of the momentum distribution Γ_{ODrCu} between the reduced OD-Cu and oxidized Cu, defined as:

$$\Gamma_{ODrCu} = (\rho_{OD-Cu} - \rho_{Cu})/\rho_{Cu} \qquad (6)$$

where ρ_{Cu} and ρ_{OD-Cu} are the momentum distributions of Cu and OD-Cu, respectively. It is clear that the fit with three terms is better compared to that with two terms.

References

(1)   Bianchi, G.; Longhi, P. Copper in Sea-Water, Potential-pH Diagrams. *Corros. Sci.* **1973**, *13* (11), 853–864.

(2)   Liu, H.; Zhou, Y.; Kulinich, S. A.; Li, J.-J.; Han, L.-L.; Qiao, S.-Z.; Du, X.-W.; Du, M.; Liu, Y.; Ji, G. Scalable Synthesis of Hollow Cu_2O Nanocubes with Unique Optical Properties via a Simple Hydrolysis-Based Approach. *J. Mater. Chem. A* **2013**, *1* (2), 302–307.

(3)   Roberts, F. S.; Kuhl, K. P.; Nilsson, A. High Selectivity for Ethylene from Carbon Dioxide Reduction over Copper Nanocube Electrocatalysts. *Angew. Chemie* **2015**, *127*, 5268–5271.

(4)   Egerton, R. F. Quantitative Analysis of Energy-Loss Data. In *Electron Energy-Loss Spectroscopy in the Electron Microscope*; Springer, 2011; pp 231–291.

(5)   Makhov, A. F. Penetration of Electrons into Solids, 1. –the Intensity of an Electron Beam, Transverse Path of Electrons. *Sov. Physics-Solid State* **1934**, *2* (9), 1961.

(6)   Veen, A. van; Schut, H.; Vries, J. de; Hakvoort, R. A.; Ijpma, M. R. Analysis of Positron Profiling Data by Means of "VEPFIT." In *AIP Conference Proceedings*; AIP, 1991; Vol. 218, pp 171–198.

(7)   Consolati, G.; Ferragut, R.; Galarneau, A.; Di Renzo, F.; Quasso, Mesoporous Materials for Antihydrogen Production. *Chem. Soc. Rev.* **2013**, *42* (9), 3821–3832.

(8)   Ivanov, I. A.; Mitroy, J. Pick-off Annihilation in Positronium Scattering from Alkali-Metal Ions. *Phys. Rev. A* **2002**, *65* (3), 34709.

(9)   Lynn, K. G.; MacDonald, J. R.; Boie, R. A.; Feldman, L. C.; Gabbe, J. D.; Robbins, M. F.; Bonderup, E.; Golovchenko, J. Positron-Annihilation Momentum Profiles in Aluminum: Core Contribution and the Independent-Particle Model. *Phys. Rev. Lett.* **1977**, *38* (5), 241–244.

(10) Dryzek, J.; Czapla, A.; Kusior, E. Positron Annihilation Studies of the Multilayer System. *J. Phys. Condens. Matter* **1998**, *10* (48), 10827–10838.

(11) Mood, A. M.; Graybill, F. A.; Boes, D. C. *Introduction to the Theory of Statistics*; McGraw-Hill, 1974.

(12) Druzhkov, A. P.; Gizhevskii, B. A.; Arbuzov, V. L.; Kozlov, E. A.; Shalnov, K. V; Naumov, S. V; Perminov, D. A. Electronic and Structural Properties of Micro-and Nanometre-Sized Crystalline Copper Monoxide Ceramics Investigated by Positron Annihilation. *J. Phys. Condens. Matter* **2002**, *14* (34), 7981–7990.

(13) Ferragut, R. Atomic Fraction around Defects Associated with Nanoparticles in AlCuMg Alloys. In *Physica B: Condensed Matter*; 2012; Vol. 407, pp 2676–2683.